P7.5   **STUDIES OF SEA SURFACE NORMALIZED RADAR CROSS SECTIONS OBSERVED BY CLOUDSAT**

Ninoslav Majurec[1], Joel T. Johnson[1], and Simone Tanelli[2]

[1] ElectroScience Laboratory, The Ohio State University, Columbus, OH
[2] Jet Propulsion Laboratory, California Institute of Technology, Pasadena, CA

1. INTRODUCTION

The primary science instrument of the CloudSat Mission is the Cloud Profiling Radar (CPR). The CPR is a W-band (94 GHz) nadir looking radar (e.g. Tanelli, 2008) with the purpose of measuring backscattered power from hydrometeors (clouds and precipitation). Although the CPR contains an internal calibration system, external calibration using geophysical sources with known normalized radar cross-section (NRCS) values is also of interest. The ocean surface can potentially serve as one such geophysical source for external calibration if an accurate understanding of the sea surface NRCS versus the sea wind speed and direction and sea surface temperature is available.

Given that CloudSat operates in a near-nadiral observation geometry, it is typically assumed that a Geometrical Optics (GO, e.g. Cox, 1954) model for sea surface scattering should be applicable. In such a model, the sea surface is entirely described by its "long wave" slope variances. These slope variances are intended to describe properties of sea waves longer than a chosen "cutoff" wavelength, usually taken as some number of electromagnetic wavelengths (3 mm at W band.) Because this cutoff wavelength is a free parameter in the GO approach, it is important to develop alternative methods to avoid this ambiguity. A recently proposed "cutoff-invariant" two-scale model (Soriano, 2008) provides predictions that are invariant to choice of the cutoff wavenumber. This presentation will describe the implementation of such a model, and the simplification of this model into a GO prediction with an appropriate cutoff wavenumber when applicable.

Predictions of the model are compared with CloudSat observations primarily for nadiral measurements but also for periodic observations at incidence angles up to approximately 15°. Required ancillary information for sea surface wind speed and sea surface temperature is obtained from the AMSR-E radiometer, and ancillary wind direction information from NCEP wind fields. Comparisons of models and CloudSat measurements are performed to assess the accuracy of existing sea spectrum models in predicting the long wave slope variances of the sea surface. Implications of the study for calibrating CloudSat measurements and for using CloudSat measurements to determine sea surface properties will be discussed.

---
[1] Ninoslav Majurec, ElectroScience Laboratory, The Ohio State University, 1320 Kinnear Rd, Columbus, OH, 43212, e-mail: majurec.1@osu.edu

2. CUTOFF INVARIANT TWO-SCALE MODEL

The two-scale model is one of the most commonly used approaches in scattering from ocean surface. In order to numerically encompass large-scale and small-scale components of the ocean surface wave spectrum, the two-scale model combines Geometrical Optics (GO) for large sea waves and the Small-Perturbation model (SPM) for small sea waves. The problem in this approach is the arbitrary choice of the dividing point between the large and small-scales and the sensitivity of the scattering cross section to this dividing point.

One solution to this problem is to replace the SPM with the first order small slope approximation (SSA, for the small-scale roughness) and use a modified GO for the large scale. The resulting NRCS predictions have been shown to be insensitive to the choice of the cutoff wavenumber, as shown by Soriano, 2008.

The small-scale rms height of the ocean surface h_S is given by

$$h_S^2 = \iint_{k>k_c} w(k_x, k_y) dk_x dk_y, \tag{1}$$

where, $w(k_x, k_y)$ is the ocean surface spectrum. Since the cutoff wavenumber k_c is usually on the order of 0.1 to 0.5 of the electrical wavenumber k_{el}, h_s tends to be small. That being the case, the SSA integral

$$\frac{e^{-Q_z^2 h^2}}{(2\pmb{p})^2 Q_z^2} \int d\bar{r} e^{-i\overline{Q_\parallel}\cdot\bar{r}} \left(e^{Q_z^2 h^2 C(\bar{r})} - 1\right) \tag{2}$$

simplifies to

$$\frac{e^{-Q_z^2 h^2}}{(2\pmb{p})^2} \int d\bar{r} e^{-i\overline{Q_\parallel}\cdot\bar{r}} h^2 C(\bar{r}) = e^{-Q_z^2 h^2} w(\overline{Q_\parallel}) \tag{3}$$

where C is the correlation function of the ocean surface. The cutoff invariant two-scale model is created from the standard two-scale model by replacing the sea spectrum in the SPM prediction (as in (3)) with the integral given in (2). This expression (when averaged over the large scale "tilt angles") then provides the solution for the local NRCS due to the small-scale part of the spectrum.

The large-scale NRCS contribution is obtained using a modified GO. The final solution is then

$$\text{GO} - \text{SSA} = \text{GO} \times e^{-Q^2 h_S^2}\left(1 - e^{-Q_z^2 h_L^2}\right) + SSA \quad (4)$$

where h_L is the large-scale rms height of the ocean surface

$$h_L^2 = \iint\limits_{k<k_c} w(k_x, k_y)\, dk_x\, dk_y \quad (5)$$

and where "SSA" refers to the SSA predictions tilted over the large wave slopes.

The code is tested for an azimuthally symmetric power law spectrum:

$$w(k_r) = \frac{a_0}{2p\, k_r^4} \quad (6)$$

Results are shown in Figures 1 and 2. The NRCS is calculated for several cutoff wavenumbers: $k_{el}/2$, $k_{el}/5$, $k_{el}/10$ and $k_{el}/20$, where

$$k_{el} = \frac{2p}{l} = \frac{2p\, f}{c} = 1968.73\ \text{rad}\big/\text{m} \quad (7)$$

for W-band (94 GHz) radar. The results (Figure 2) confirm that the predictions of the model are insensitive to the choice of the cutoff wavenumber, even though the individual GO and SSA parts of the model are varying significantly with the cutoff.

The Cutoff Invariant Two-scale code uses an azimuthally dependent ocean surface spectrum of the form

$$w(k, j) = w_0(k) + w_2(k)\cos(2j) \quad (8)$$

For this type of spectrum computation of the local SSA NRCS requires only the solution of two 1D integrals (in polar coordinates):

$$P_0 = \frac{e^{-Q_z^2 h_S^2}}{2p}\int_0^\infty \left[e^{Q_z^2 h_S^2 C_0(r)} - 1\right] J_0(k_r r)\, r\, dr \quad (9)$$

$$P_2 = -Q_z^2 h_S^2\, \frac{e^{-Q_z^2 h_S^2}}{2p}\int_0^\infty C_2(r)\, e^{Q_z^2 h_S^2 C_0(r)}\, J_2(k_r r)\, r\, dr \quad (10)$$

where

$$C(r, j) = C_0(r) + C_2(r)\cos(2j) \quad (11)$$

is the azimuthally dependent correlation function of the ocean surface.
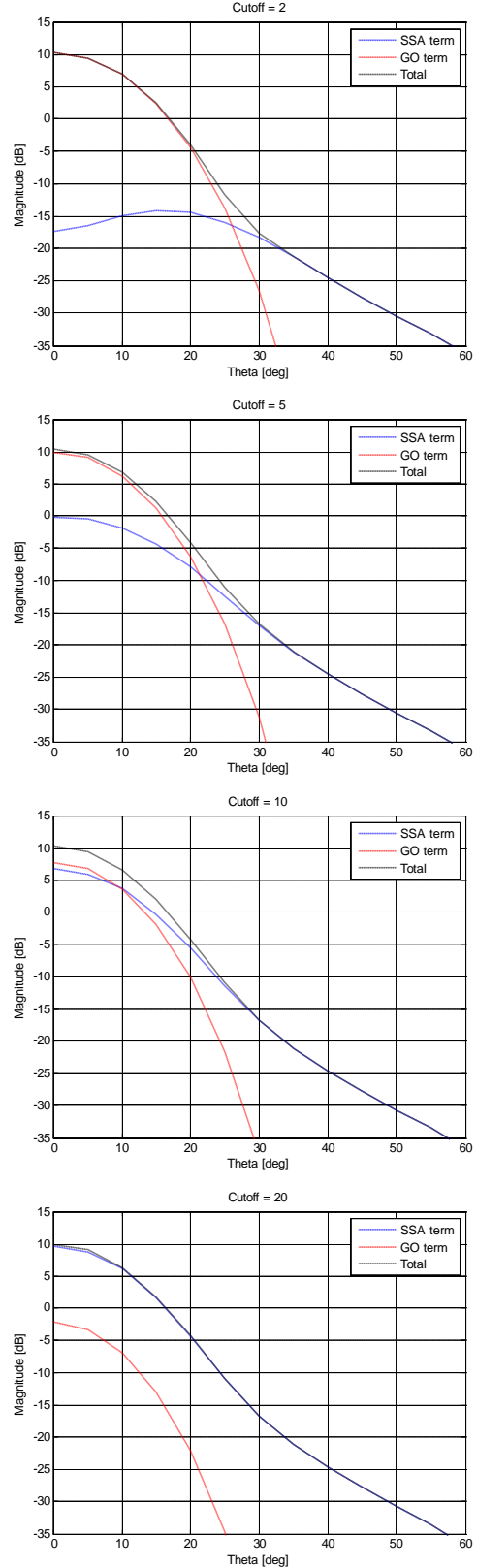
Figure 1 *Comparison of the NRCS calculations using cutoff invariant two-scale model for radially symmetric ocean surface spectrum.*

2
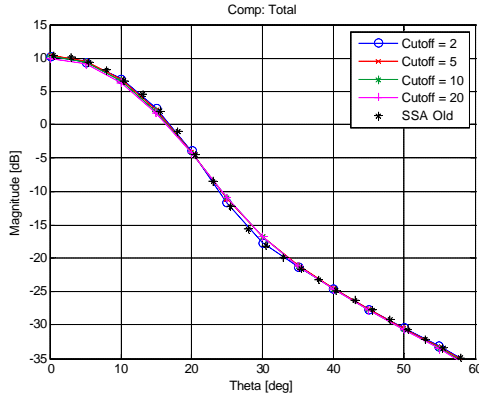
Figure 2 *Comparison of the cutoff invariant two-scale model results.*

The code implementing two-scale cutoff-invariant model consists of the two parts that are run in sequence. The first part calculates the azimuthally dependent correlation function using a selected ocean surface spectrum model (e.g. Durden-Vesecky, Elfouhaily). This correlation function is then used to calculate P_0 and P_2 according to (9) and (10) for a set of incidence angles spanning 0 to 90 degrees. Input parameters are the radar frequency, wind speed, and choice of a cutoff wavenumber (note this choice is required even though the model's predictions eventually do not vary with this choice). Calculated values for C_0 and C_2 are saved as an intermediate result. The results of this first part of the code are the tabulated P_0 and P_2 integrals, which are used to compute the "facet" SSA NRCS in the "tilting" process performed by the second part of the code.

The second part of the code thus takes the pre-calculated P_0 and P_2 tables and computes the modified GO and tilted SSA cross sections which are summed to obtain the total ocean surface NRCS. Inputs are the frequency, wind speed, wind azimuth, sea surface temperature, incidence angle(s), choice of the surface spectrum model (Durden-Vesecky, Elfouhaily), and choice of the model for the dielectric constant of the sea water (e.g. Klein, 1977, Ellison, 1998 or Meissner, 2004).

In order to expedite comparisons with measured data, the code can be used to create a table of NRCS values for a range of input parameters, here chosen as the 5 dimensional array:

1. Sea surface temperature from 5 to 30 ºC with a step of 5 ºC
2. Wind speed form 3 to 15 m/sec with a step of 1.5 m/sec
3. Wind azimuth from 0º to 360º with a step of 10º
4. Incidence angle from 0º to 60º with a step of 2º
5. Products: 1 – GO only,
                     2 – H polarization,
                     3 – V polarization,
                     4 – Cross-Polarization.

These tables can be computed for varying spectrum and dielectric constant models, and then used as lookup tables in comparing model predictions with observed data. A 5D interpolation of tabulated values is performed in this process to provide model predictions for the ground truth data associated with a given observation. This process is by far faster than evaluating the cutoff invariant two-scale model for each data point. As an example, Figure 3 provides an illustration of W-band HH NRCS values versus incidence angle and wind azimuth at wind speed 12 m/s and SST 20 ºC using the Durden-Vesecky spectrum and the Ellison dielectric constant model. The results show the expected rapid decay in NRCS values with incidence angle, as well as the increasing impact of wind direction as the incidence angle becomes larger.
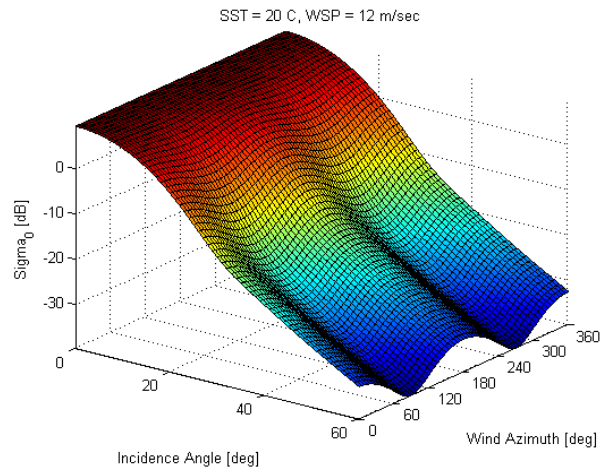
Figure 3 *Ocean surface s_0 (H-pol) vs. incidence angle and wind azimuth for W-band (94 GHz) using Durden-Vesecky surface spectrum and Ellison dielectric constant model.*
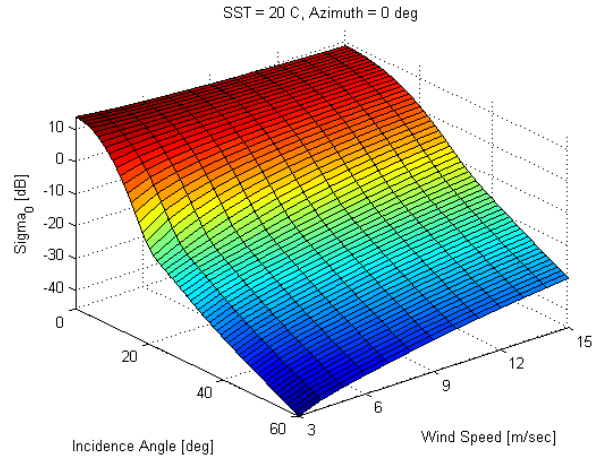
Figure 4 *Ocean surface s_0 (H-pol) vs. incidence angle and wind speed for W-band (94 GHz) using Durden-Vesecky surface spectrum and Ellison dielectric constant model.*

Figure 4 is similar, but plotted versus incidence angle and wind speed for up-wind observations; the results show the transition that occurs in sea scattering from a

3

decreasing NRCS versus wind speed in nadiral measurements, to an increasing NRCS with wind speed at larger incidence angles.

The Cutoff Invariant Two-Scale code can also be used to verify the applicability of simpler models, such as the GO. The fact that the model's predictions are insensitive to choice of the cutoff wavenumber was demonstrated (see Figures 1 and 2). Figure 1 illustrates the individual contributions of the "tilted" SSA and GO portions of the model to the total NRCS when the cutoff wavenumber is equal to $k_{el}/2$ (top) to $k_{el}/20$ (bottom). The top plot confirms that, for incidence angles less than ~15 degrees, the GO portion of the model is dominant if one chooses the cutoff wavenumber to be $k_{el}/2$. Therefore the more complicated cutoff invariant two-scale model has confirmed that it is justified to use a much simpler model (the GO alone) for near nadiral observations if the cutoff wavenumber is taken as $k_{el}/2$. For such a model, the surface is completely described in terms of its up and cross wind long-wave slope variances.

3. CLOUDSAT DATA ANALYSIS

3.1 Nadir looking data points

The CloudSat dataset under consideration consists of 2770 granules (orbits). These 2770 granules can be subdivided into nine groups by their time continuity, as listed in Table 1. The data analysis was done in several steps. First, the complete data files were reduced by selecting points relevant for the analysis of the sea surface NRCS; such points must

1. be over the ocean (*surf_lof* = 2, land-ocean flag)
2. have a clear echo (*cpr_type* = 1)
3. have no NaNs in *s0ms*
4. have no NaNs in *amsr_gasatt*
5. have no NaNs in *amsr_wsp*
6. have no NaNs in *ncep_windaz*, and
7. have no NaNs in *amsr_sst*

Table 1 *List of data file groups according to time continuity.*

Group	Granules	Length	Time
1	01379-02058	679 files ~47 days	2006/08/01 (213) 00:57:18 2006/09/16 (259) 16:00:13
2	06446-06912	467 files ~32 days	2007/07/14 (195) 23:43:40 2007/08/15 (227) 23:43:43
3	06923	1 file 01:38:52	2007/08/16 (228) 17:51:27 2007/08/16 (228) 19:30:19
4	08034-08295	262 files ~18 days	2007/11/01 (305) 00:51:10 2007/11/18 (322) 23:00:00
5	08879-09154	275 files ~19 days	2007/12/29 (363) 01:28:16 2008/01/16 (016) 22:41:38
6	09869-10115	247 files ~17 days	2008/03/06 (066) 01:03:50 2008/03/22 (082) 22:29:18
7	10495-10785	289 files ~20 days	2008/04/18 (109) 04:54:44 2008/05/07 (128) 22:42:17
8	13073-13173	100 files ~7 days	2008/10/12 (286) 01:30:48 2008/10/18 (292) 22:19:17
9	14253-14703	450 files ~31 days	2009/01/01 (001) 02:15:30 2009/01/31 (031) 23:54:05

Points that satisfy these conditions were collected into separate files that contain only the surface reflectivity (*s0ms*), 2-way gas attenuation (*amsr_gasatt*), latitude (*lats*), longitude (*lons*), time stamp from Jan 1 1993, 0000Z (*TAI_ray_time*), wind speed (*amsr_wsp*), wind direction (*ncep_windaz*), and sea surface temperature (*amsr_sst*). These points were then collected into larger files for each of the time blocks shown in Table 1. Data from each time block was then binned into a 3D array by:

1. Sea surface temperature from 0 to 30 °C with bin size 1 °C,
2. Wind speed from 0 to 30 m/sec with bin size 0.5 m/sec,
3. Wind direction from 0° to 360° with bin size 5°

Figure 5 illustrates histograms of the sea surface temperature (a), wind speed (b), and wind direction (c) for Group 1 (Granules 01379-02058, Aug-Sept 2006). The plots illustrate the predominance of higher sea surface temperature datapoints for this time period, as well as the expected near Rayleigh distributed wind speeds and wind directions associated with zonal flow. The small uptick in the wind speed histogram for wind speeds near 30 m/s is believed to be an error in the ground truth information. Figure 6 plots similar normalized histograms for all groups except group 3 (single file), and shows similar behaviors to those of Figure 5.

The top plot in Figure 7 illustrates the Group 1 NRCS vs. wind speed and sea surface temperature (NRCS is averaged over all wind directions.) The corresponding number of points used to produce this plot is shown in the bottom plot. A large number of points (10,000 or more) is available for moderate wind speeds (around 6 m/sec) and SST above 10 °C. For lower SST, wind speeds above ~15 m/sec apparently have an insufficient number of points to produce a useful average. At high SST, σ_0 appears to have a minimum around 15 m/sec and then to increase for higher wind speeds; this is contrary to any model used, and possibly again a result of an insufficient number of observations at the higher wind speeds.

NRCS averages versus wind direction and wind speed (averaged over all SST values) in the upper plot in Figure 8 similarly show the effects of an insufficient number of points in some wind directions and at higher wind speeds. However, the expected independence of nadiral observations on the wind direction is observed. In general, these plots suggest portions of binned CloudSat nadiral observations to utilize for further comparisons with models. Figures 9 and 10 are analogous to Figures 7 and 8, but for the Group 9 dataset. They show similar behaviors.
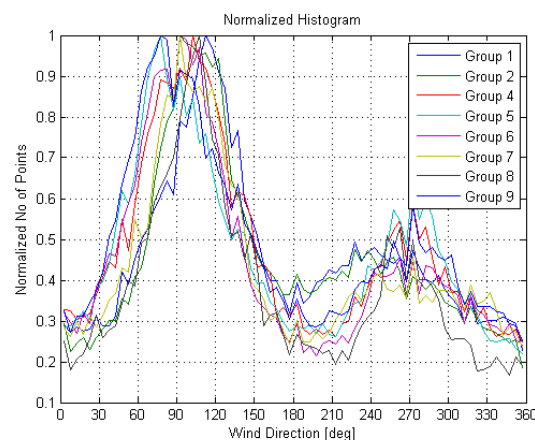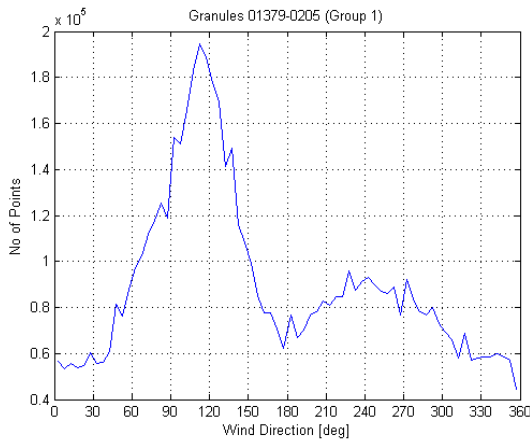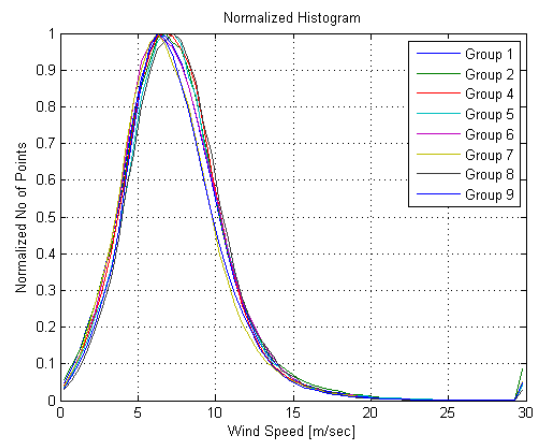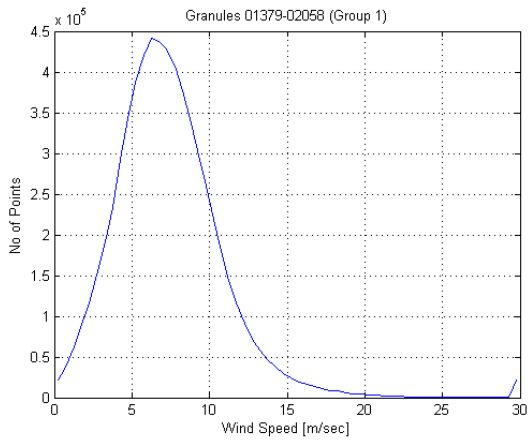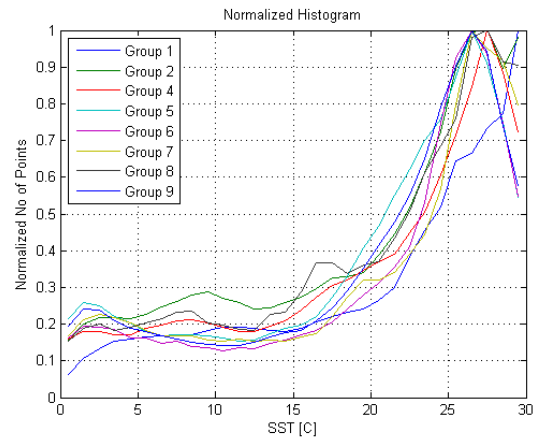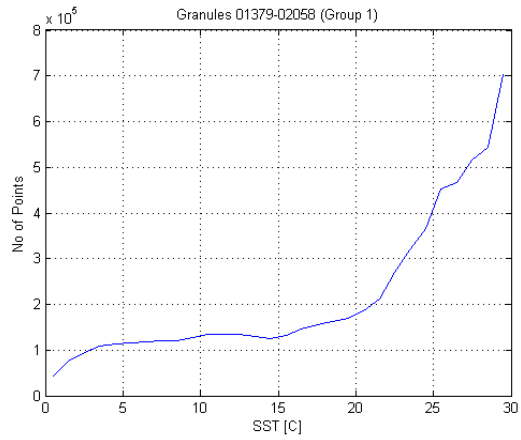
Figure 5 *Histograms for Granules 01379-02058 (Group 1) against sea surface temperature, wind speed and wind direction.*

Figure 6 *Normalized histograms for all groups. All groups seem to exhibit similar behavior.*

Granules 14253-14703 (Group 1)

Granules 14253-14703 (Group 1)
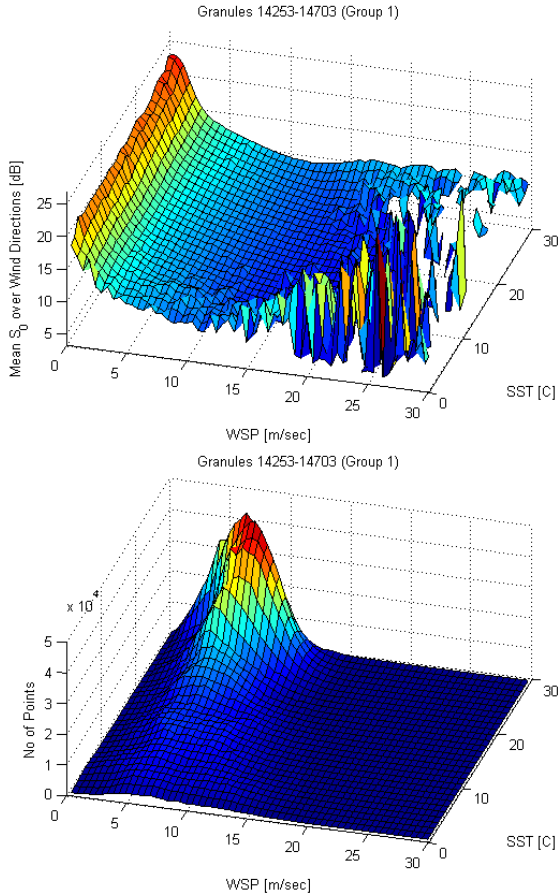
Figure 7 *Mean surface reflectivity for Group 1 over all wind directions (top) and corresponding number of available data points (bottom).*

Figure 11 plot σ_0 averaged over wind direction vs. wind speed for Group 1 (top) and Group 9 (bottom) for low (10-11 °C), medium (20-21 °C) and high (27-28 °C) SST bins. Both groups show similar averages even though they were collected almost three years apart.

The CloudSat data from Figure 11 are compared with cutoff-invariant model predictions in Figures 12 (Group 1) and 13 (Group 9). Models predictions are shown for the following cases:

1. Durden-Vesecky ocean surface spectrum model with original amplitude (a_0 = 0.004) and Ellison et al [8] sea water dielectric constant model,
2. Elfouhaily spectrum with Ellison sea water dielectric constant model,
3. Elfouhaily spectrum with Klein-Swift sea water dielectric constant model,
4. Durden-Vesecky spectrum with double original amplitude (a_0 = 0.008) and Ellison sea water dielectric constant model
5. Durden-Vesecky spectrum with 1.5 original amplitude (a_0 = 0.006) and Ellison sea water dielectric constant model

6. Durden-Vesecky spectrum with 1.347 amplitude (a_0 = 0.00539) and Ellison sea water dielectric constant model
7. GO using Cox-Munk (1954) slopes with Ellison sea water dielectric constant model
8. GO using Cox-Munk slopes with Klein-Swift sea water dielectric constant model

Granules 14253-14703 (Group 1)

Granules 14253-14703 (Group 1)
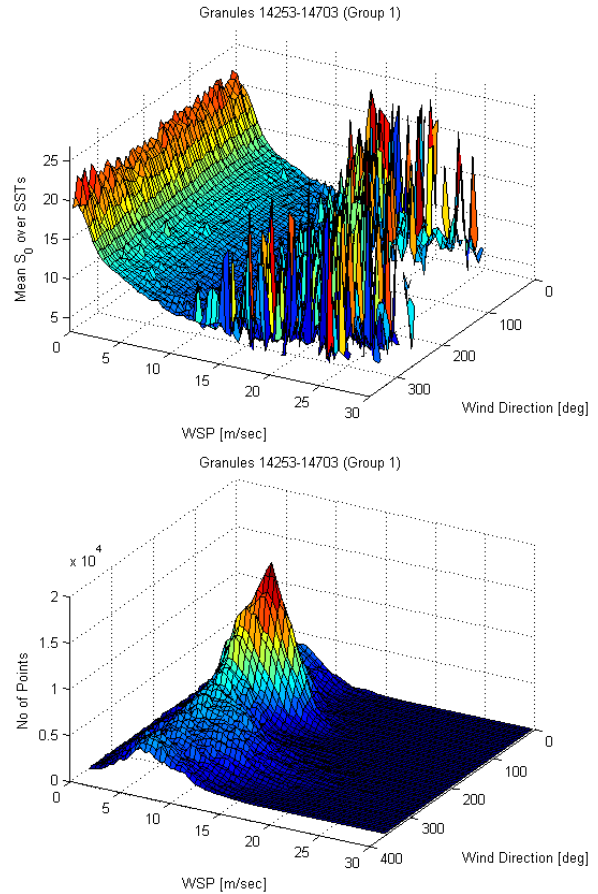
Figure 8 *Mean surface reflectivity for Group 1 over all sea surface temperatures (top) and corresponding number of available data points (bottom).*

At low sea surface temperatures (10-11 °C), the GO using Cox-Munk slopes seems to match the data for wind speeds from 3 to 15 m/sec, with a slight overestimation. The Elfouhaily spectrum and Durden-Vesecky with a_0 = 0.00539 also match the data in a somewhat smaller range of wind speeds (8-15 m/sec). As the SST is increased, models using the Klein-Swift dielectric description follow the data more closely, although at the highest SST, even this model results in a slight underestimation of the observed NRCS values. Similar results are obtained in both Figures 12 and 13, given the similarity of the two datasets shown in Figure 11.

6
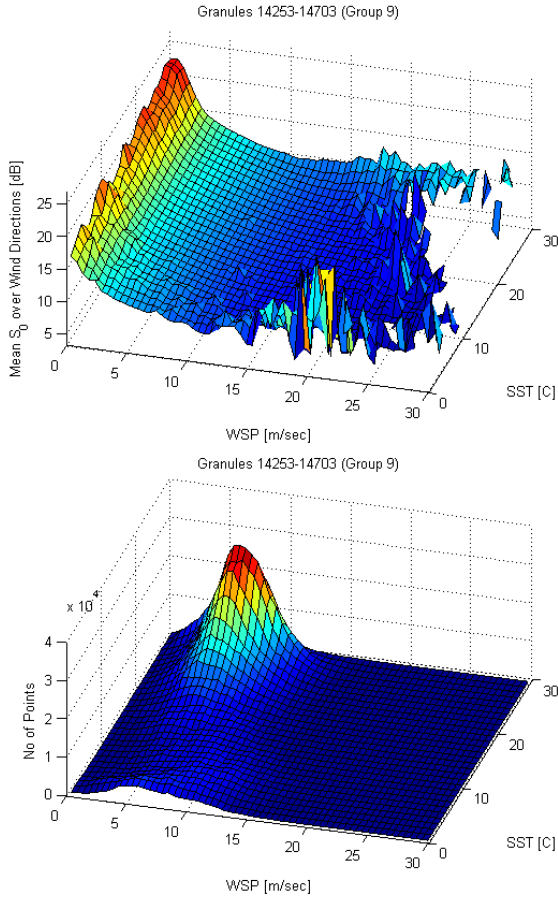
Figure 9 *Mean surface reflectivity for Group 9 over all wind directions (top) and corresponding number of available data points (bottom).*
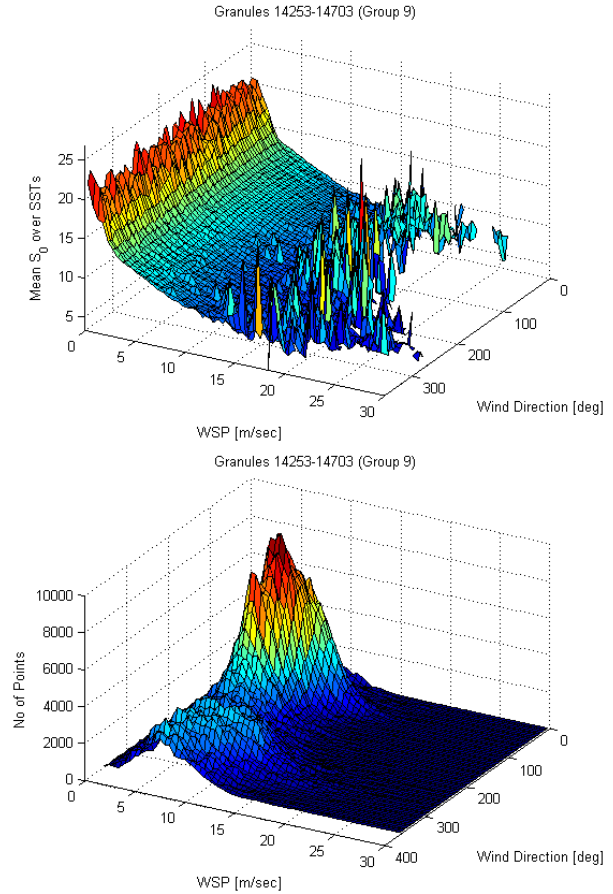
Figure 10 *Mean surface reflectivity for Group 9 over all sea surface temperatures (top) and corresponding number of available data points (bottom).*

Note that for the GO model with Cox-Munk slopes used here, the factor C_l (see equation (8) in Majurec, 2008) is set to 1. This factor models the reduction in the facet reflectivity due to the presence of roughness at wavenumbers larger than the cutoff wavenumber (i.e. shorter than 6 mm for W band using $k_{el}/2$), and is included in the GO portion of the cutoff-invariant model. A variety of C_l values have been used in the literature (e.g. 0.88 in Li, 2005). However, calculated values of C_l (according to Majurec, 2008 equation 8 and Figure 2) are much closer to 1 than to 0.88 for cutoff wavenumber $k_{el}/2$, so that the use of $C_l = 1$ is justified. It has been already stated that the Cutoff Invariant Two-scale model value for cutoff $k_{el}/2$ and low incidence angles is dominated by the GO term. The success of the Cox-Munk model in matching CloudSat nadiral NRCS values implies that the optically measured Cox-Munk sea slope variances are good approximations for the "long wave" surface slope variance at W-band (see Apel, 1994 section 3.1.3.); this is equivalent to stating that the contributions of sea waves shorter than 6 mm to the optical surface slope variance is not significant.

These comparisons have motivated a more careful examination of the dielectric constant models utilized, as shown in Figure 14. The plot illustrates the normal incidence reflectivity that is included in the GO model. The best match of the simulation and data across temperature (Figures 12 and 13) is achieved by the Klein-Swift dielectric constant model, due to the increased reflectivity obtained at high SST values. The Ellison model provides a slightly improved match for mid-temperatures, but considerably underestimates NRCS values for the high temperatures. The Meissner-Wentz model overestimates at lower temperatures much more than any other model, and also predicts smaller reflectivities than Klein-Swift at high SST.

Note that none of the dielectric models claim to be accurate at 94 GHz. Furthermore, choosing the Klein-Swift dielectric constant model based solely on its match to high temperature data may not be justified, since the high surface reflectivity values at such SSTs may originate from causes other than the dielectric constant alone. This aspect will probably need further work. Nevertheless, these studies have shown that the GO using Cox-Munk slope variances with C_l =1 provides a reasonable agreement with CloudSat nadiral observations.
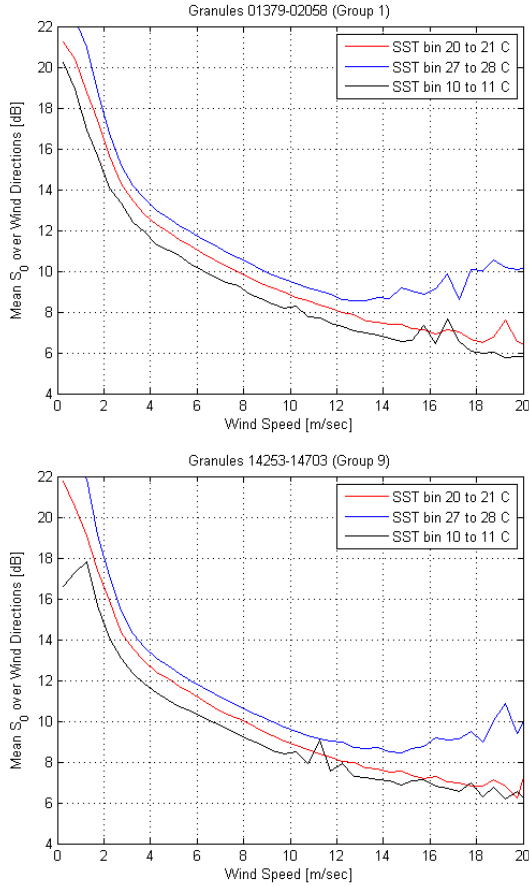
Figure 11 *Mean s_0 over all wind directions vs. wind speed for Group 1(left) and Group 9 (right). Three SST bins are chosen for comparison with the models.*

3.2 Calibration maneuvers (off nadir)

Within the CloudSat dataset provided, there are nine calibration maneuvers (Table 2).

Table 2 *Calibration maneuvers available in the dataset*

Man	Granule	Time	Comment
1	01405	2006/08/02 (214) 19:48:19	Bit cloudy, S India, Lat S11 to S34, Inc Ang. -11.118º to -11.132º
2	02040	2006/09/15 (258) 10:20:17	Bit cloudy, Mid Pac, Lat S00 to S23, Inc Ang. 11.125º to 11.135º
3	06505	2007/07/19 (200) 00:57:51	Clear, S Atlantic, Lat S00 to S35, Inv Ang. -11.12º to -0.32º
4	06923	2007/08/16 (228) 17:51:27	Bit Cloudy, W Aust, Lat S12 to S43, Inc Ang. 0.32º to 11.12º
5	08059	2007/11/02 (306) 18:03:17	Cloudy, W Aust, Lat S12 to S43 Very few points left
6	09123	2008/01/14 (014) 19:36:12	Clear, E India, Lat N23 to N06
7	09124	2008/01/14 (014) 21:05:05	Leftover of 09123
8	10782	2008/05/07 (128) 17:45:38	Clear, Longer, NW Aust, S09 to S39
9	13112	2008/10/14 (288) 17:47:17	2 sections, W Aust, S09 to S39
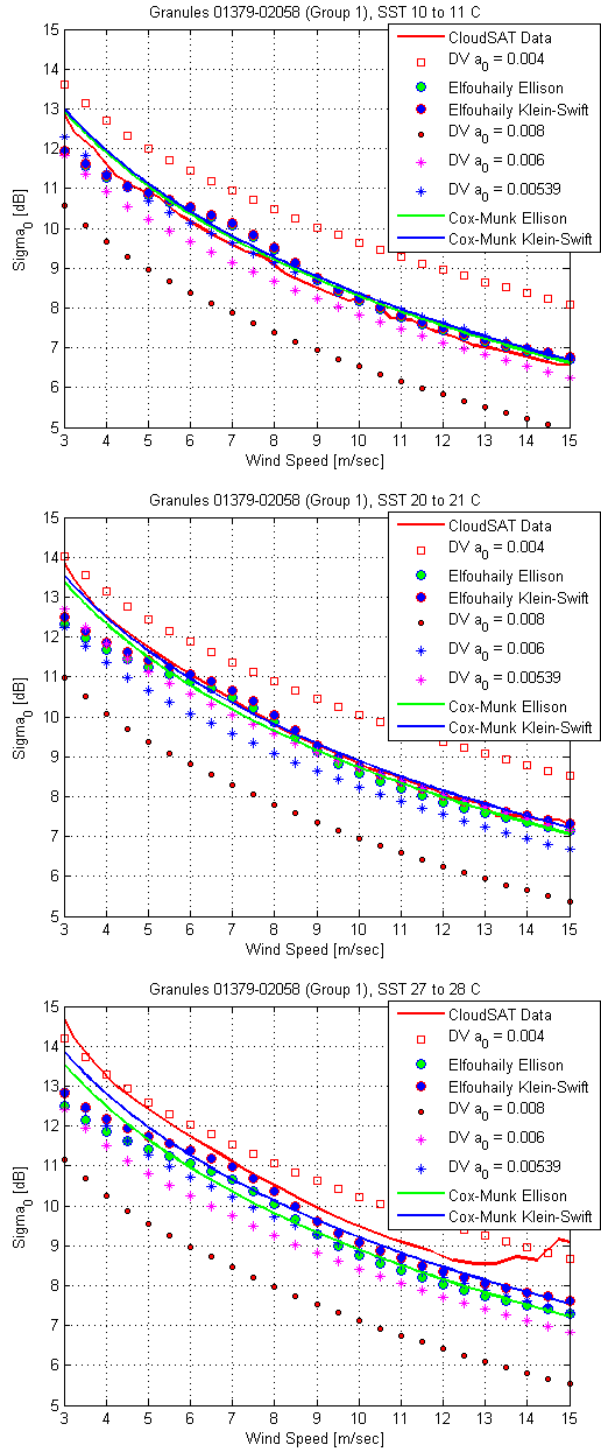
Figure 12 *Comparison of the Group 1 data to the various models for the ocean surface scattering. Sea surface temperature bin 10-11 °C (top plot), 20-21 °C (middle plot) and 27-28 °C (bottom plot).*

8
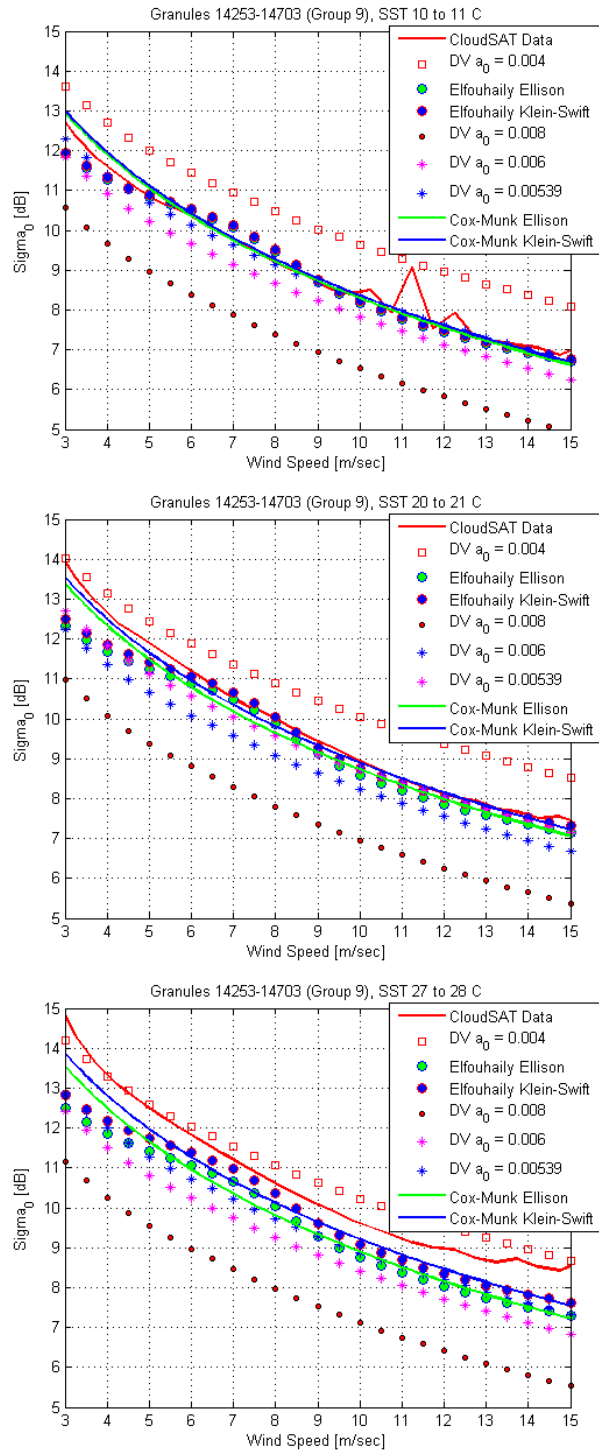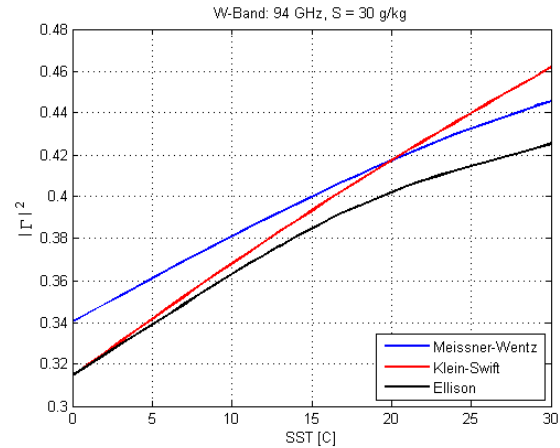
Figure 14 *Normal incidence reflectivity (Factor **G**) derived from the dielectric constant for sea water vs. sea surface temperature according to Klein-Swift (1954), Ellison et al. (1998) and Meissner-Wentz (2004).*

The first two maneuvers were not analyzed further because they include observations only at one angle whereas the software developed for this analysis generates bins in incidence angle. Maneuver 7 (the completion of Maneuver 6) includes significant cloud and rain regions, and therefore was also not analyzed. Maneuvers 3, 4, and 5 are also omitted, due to the periods of a constant incidence angle. Such constant angle periods may be more naturally analyzed using methods similar to those used for the nadiral case. The remaining calibration maneuver datasets were analyzed separately for each maneuver.

The following process identified calibration maneuvers:

1. Search through data files for *cpr_type* >= 10 to identify calibration periods,
2. A range of incidence angles were manually chosen from *surf_sci* variables that satisfy 1,
3. Within the selected range of points, records with *cpr_type* = 11 were chosen. This would identify clear calibration periods and, at the same time, eliminate bad or cloudy periods.
4. An additional check for land/ocean was done manually, since flag *surf_lof* does not work during calibration periods.

The resulting data values are compared to several models:

1. Durden-Vesecky ocean surface spectrum model with original amplitude ($a_0 = 0.004$) and Ellison sea water dielectric constant model,
2. Elfouhaily spectrum with measured wind azimuth and Ellison sea water dielectric constant model,
3. Elfouhaily spectrum with mean wind azimuth and Ellison sea water dielectric constant model,
4. Durden-Vesecky spectrum with double original amplitude ($a_0 = 0.008$) and Ellison sea water dielectric constant model

Figure 13 *Comparison of the Group 9 data to the various models for the ocean surface scattering. Sea surface temperature bin 10-11 °C (top plot), 20-21 °C (middle plot) and 27-28 °C (bottom plot).*

9

5. Durden-Vesecky spectrum with 1.5 original amplitude (a_0 = 0.006) and Ellison sea water dielectric constant model
6. Durden-Vesecky spectrum with 1.347 amplitude (a_0 = 0.00539) and Ellison sea water dielectric constant model
7. GO using Cox-Munk slopes with Klein-Swift sea water dielectric constant model

Calibration maneuvers 6, 8, and 9 were analyzed first. After comparisons with the cutoff-invariant model using the Durden-Vesecky ocean surface spectrum with its original amplitude (a_0 = 0.004), double amplitude (a_0 = 0.008), and 1.5 times original amplitude (a_0 = 0.006), the value a_0 = 0.00539 was determined to produce the best match for maneuvers 6, 8, and 9.
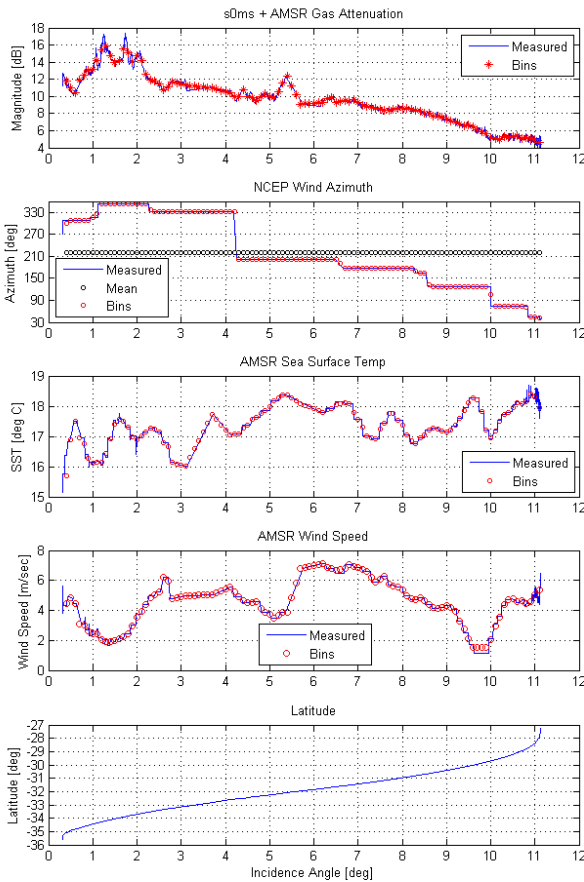
Figure 15 *Calibration period within Granule 6505. This is the case with low to moderate wind speeds and low SST. Plots show, top to bottom: measured s_0, NCEP wind azimuth, AMSR Sea surface temperature, AMSR wind speed and latitude of the footprint during the calibration maneuver.*
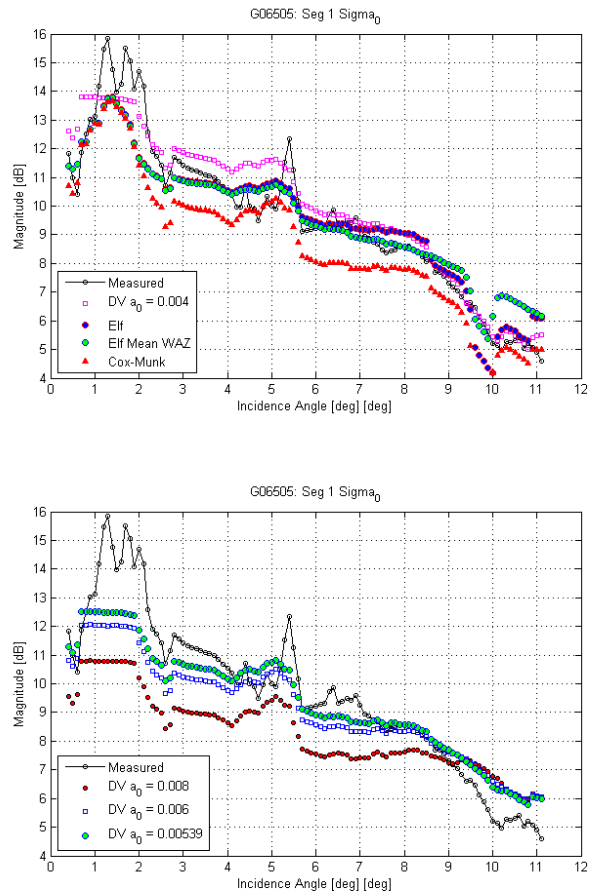
Figure 16 *Comparison between the measured values ad the model predictions for the calibration period within Granule 6505. Top plot shows comparison with Durden-Vesecky ocean surface spectrum, Elfouhaily with measured wind azimuth, Elfouhaily with mean wind azimuth and GO using Cox-Munk slopes. Durden-Vesecky model shows good agreement with the measured data, especially for incidence angles above 6 degrees. Elfouhaily shows good agreement down to 3 degrees. Area under 2 degrees is not accurate, since the model was limited for wind speed above 3 m/sec. Durden-Vesecky models with higher amplitudes (bottom plot) do not follow the shape of the data very well.*

10

Example comparisons of the data with the models are shown in Figures 15 to 20, each of which represents one calibration maneuver as specified in the Figure caption. The data is separated into 0.1º bins according to the incidence angle. The Figures 15, 17 and 19 contain, from top to bottom,

1. the measured NRCS (*s0ms*) corrected for the gas attenuation (*amsr_gasatt*),
2. the NCEP predicted wind azimuth (*ncep_windaz*),
3. the AMSR sea surface temperature (*amsr_sst*),
4. the AMSR wind speed (*amsr_wsp*),
5. the latitude corresponding to the measurement point (*lats*)

while the Figures 16, 18 and 20 show the comparison between the data and the models. For clarity, the comparison chart is split into two plots, with the upper containing the optimized Durden-Vesecky, Elfouhaily, Elfouhaily with mean wind azimuth and Cox-Munk predictions, while the lower illustrates the impact of the Durden-Vesecky spectrum amplitude.
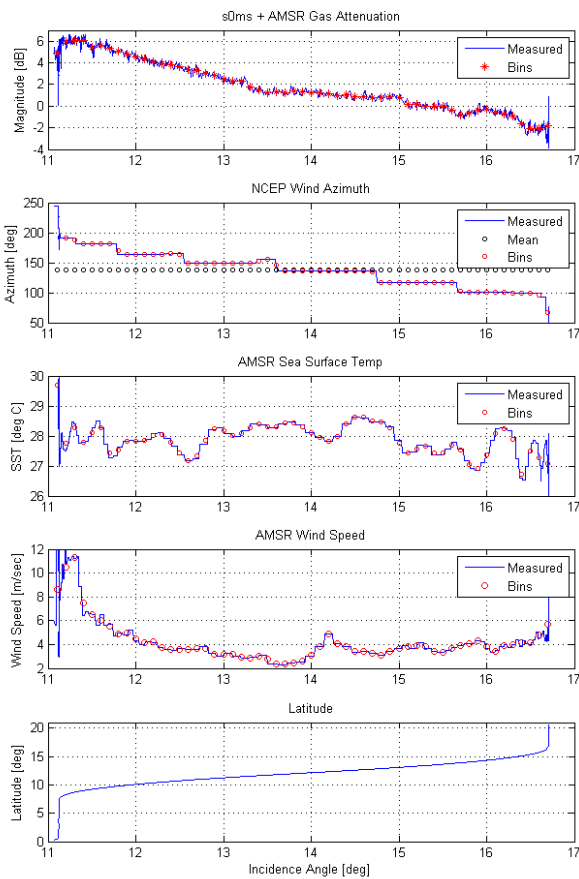
Figure 17 *Calibration period within Granule 9123. This is the case with low wind speeds and high SST. Plots show, top to bottom: measured $\mathbf{s}_0$, NCEP wind azimuth, AMSR Sea surface temperature, AMSR wind speed and latitude of the footprint during the calibration maneuver.*
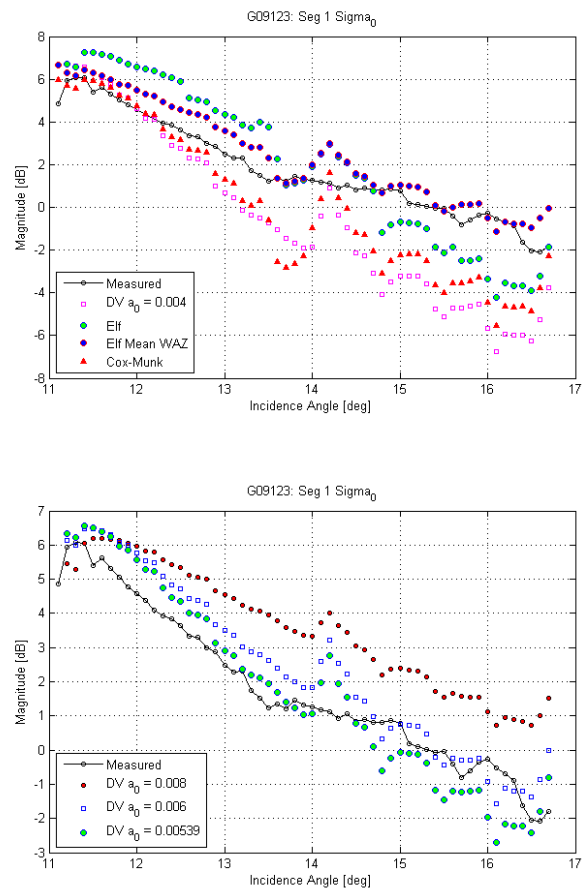
Figure 18 *Comparison between the measured values ad the model predictions for the calibration period within Granule 9123. In this case it is evident that the Elfouhaily spectrum has somewhat too strong dependence on wind azimuth. This is reported in the literature, but further investigation is needed. Durden-Vesecky spectrum with ($a_0 = 0.00539$) shows fairly reasonable agreement with the data. Standard Durden-Vesecky spectrum shows considerable underestimation for wind speeds less than 5 m/sec.*

11
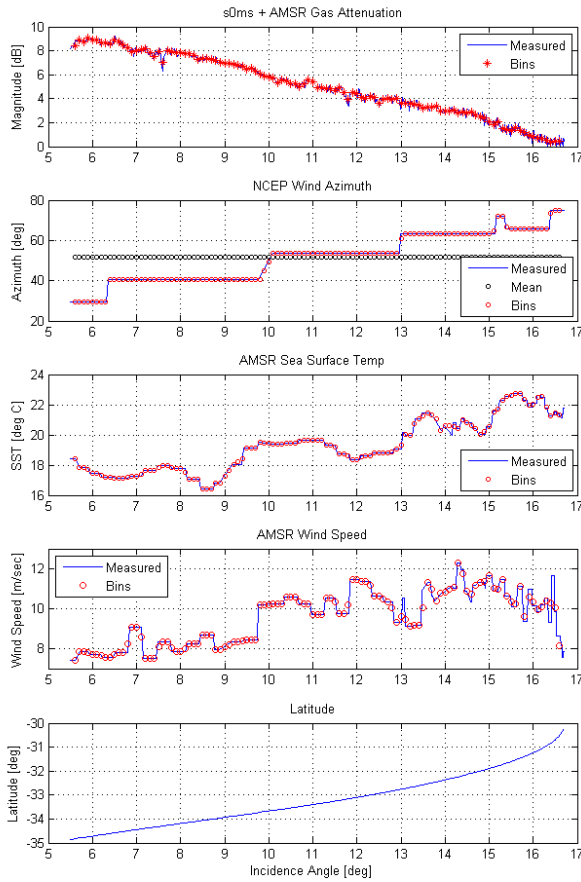
Figure 19 *Segment 2 of the calibration period within Granule 13112. This is the case with high wind speeds and medium SST. Plots show, top to bottom: measured s_0, NCEP wind azimuth, AMSR Sea surface temperature, AMSR wind speed and latitude of the footprint during the calibration maneuver.*

Figure 20 *Comparison between the measured values ad the model predictions for the segment 2 of the calibration period within Granule 13112. Durden-Vesecky spectrum with*

$a_0 = 0.004$ seem to capture the measured values reasonably well. There is especially good agreement for incidence angles from 13 to 17 degrees. On the other hand, Elfouhaily spectrum behaves better for low incidence angles, as well as Durden-Vesecky spectrum with $a_0 = 0.00539$.

These plots are just a few examples, and are somewhat difficult to interpret due to the varying wind speeds, wind directions, and sea surface temperatures as the incidence angle is increased. Continued analysis is in progress, and obtaining a larger set of calibration maneuver records would be useful to attempt to form a binned product in wind speed and SST for all incidence angles. Note an excessive dependence on the wind azimuth of the Elfouhaily ocean surface spectrum has been noticed; this problem could be addressed in the future perhaps by replacing the azimuthal spreading function of the Elfouhaily spectrum with an alternate form.

4. CONCLUSIONS

The Cutoff Invariant Two-scale code has been used with a number of ocean surface spectral models (three versions of the Durden-Vesecky model and the Elfouhaily model). One foreseeable new model to be implemented is a modified Elfouhaily model with weaker wind azimuth dependence.

The Cutoff Invariant Two-scale code was used to investigate the quality and applicability of simpler methods, such as the traditional GO. The results have shown that $k_e/2$ is an appropriate cutoff choice for the GO approximation, and that the GO alone is sufficiently

accurate under this choice for NRCS predictions at incidence angles up to approximately 15 degrees.

An extensive analysis of CloudSat nadiral sea NRCS values was performed. There are several important results of this analysis:

1. The stability of the CloudSat system. The analyzed data set spans the period of nearly three years, during which very similar average values for the CloudSat NRCS versus wind speed are obtained.
2. Use of the GO model with Cox-Munk slope variances appears to provide good predictions for nadiral points at low to moderate sea surface temperatures. This apparently demonstrates that the "long wave" slope variance at W-band approaches the optical Cox-Munk limit.
3. The Klein-Swift model appears to provide the best prediction of the sea water dielectric constant over a wide range of SST values.
4. Increased differences between models and measurements are observed at high SSTs. It is not clear if this is due to inaccuracies in the dielectric constant models or some other phenomenon.

Initial analysis of the CloudSat calibration maneuver was also presented. These cases have a much smaller number of data points compared to the nadiral case, and therefore a larger dataset will be valuable for future studies. The calibration maneuver example datasets considered showed that a modified Elfouhaily surface spectrum model with weaker wind azimuth dependence may be valuable for the future, as well as investigations of the GO/Cox-Munk approach.

5. ACKNOWLEDGEMENTS

REFERENCES

Apel, J. R., 1994: An Improved Model for the Ocean Surface Wave Vector Spectrum and its Effects on Radar Backscatter, *Journal of Geophysical Research*, Vol. 99, No. C8, pp. 16269-116291.

Cox, C. and Munk, W., 1954: Measurements of the roughness of the sea surface from photographs of the sun's glitter, *J. Opt. Soc. Amer.*, 144, pp. 838-850.

Durden, S. L. and Vesecky, J. F., 1985: A physical radar cross-section model for a wind-driven sea with swell, *IEEE Journal of Oceanic Eng.*, Vol. 10, No. 4, pp. 445-451.

Elfouhaily, T., Chapron, B., Katsaros, K., Vandemark, D., 1997: A Unified Directional Spectrum for Long and Short Wind-Driven Waves, *Journal of Geophysical Research*, Vol. 102, No. C7, pp. 15781-15796.

Ellison, W. et al, 1998: New Permittivity Measurements of Seawater, *Radio Science*, Vol. 33, No. 3, pp. 639-648.

Klein, L. A. and Swift, C. T., 1977: An Improved Model for the Dielectric Constant of Sea Water at Microwave Frequencies, *IEEE Transactions on Antennas and Propagation*, Vol. AP-25, No. 1.

Li, L. et al., 2005: Measurements of ocean surface backscattering using an airborne 94-GHz cloud radar - implication for calibration of airborne and spaceborne W-band radars, *J. Atmospheric Oceanic Technology*, vol. 22, 1033-1045.

Majurec, N. and Johnson, J. T., 2008: Geometrical Optics Analysis of the W-band Ocean Surface Radar Backscatter Cross Section, JPL Report.

Majurec, N. and Johnson, J. T., 2009: Cutoff Invariant Two-Scale Model of the W-band Ocean Surface Radar Backscatter Cross Section, JPL Report.

Meissner, T. and Wentz, F. J., 2004: The Complex Dielectric Constant of Pure and Sea Water From Microwave Satellite Observations, *IEEE Transaction on Geoscience and Remote Sensing*, Vol. 42, No. 9.

Soriano, G. and Guérin C. A., 2008: A Cutoff Invariant Two-Scale Model in Electromagnetic Scattering From Sea Surface, *IEEE Geoscience and Remote Sensing Letters*, Vol. 5, No. 2, pp. 199-203.

Tanelli, S., S. L. Durden, E. Im, K. S. Pak, D. G. Reinke, P. Partain, J. M. Haynes, and R. T. Marchand, 2008: CloudSat's Cloud Profiling Radar after 2 years in orbit: performance, calibration, and processing, *IEEE Transaction on Geoscience and Remote Sensing*, Vol. 46, No. 11, Part 1, pp. 3560-3573.